Space Radiation and Human Exposures, A Primer

Author: Nelson, Gregory A.

Source: Radiation Research, 185(4) : 349-358

Published By: Radiation Research Society

URL: https://doi.org/10.1667/RR14311.1

RADIATION RESEARCH **185**, 349–358 (2016)
0033-7587/16 $15.00

DOI: 10.1667/RR14311.1

Space Radiation and Human Exposures, A Primer

Gregory A. Nelson

Department of Basic Sciences, Division of Radiation Research, Loma Linda University, Loma Linda, California 92354

Nelson, G. A. Space Radiation and Human Exposure, A Primer. *Radiat. Res.* 185, 349–358 (2016).

The space radiation environment is a complex field comprised primarily of charged particles spanning energies over many orders of magnitude. The principal sources of these particles are galactic cosmic rays, the Sun and the trapped radiation belts around the earth. Superimposed on a steady influx of cosmic rays and a steady outward flux of low-energy solar wind are short-term ejections of higher energy particles from the Sun and an 11-year variation of solar luminosity that modulates cosmic ray intensity. Human health risks are estimated from models of the radiation environment for various mission scenarios, the shielding of associated vehicles and the human body itself. Transport models are used to propagate the ambient radiation fields through realistic shielding levels and materials to yield radiation field models inside spacecraft. Then, informed by radiobiological experiments and epidemiology studies, estimates are made for various outcome measures associated with impairments of biological processes, losses of function or mortality. Cancer-associated risks have been formulated in a probabilistic model while management of non-cancer risks are based on permissible exposure limits. This article focuses on the various components of the space radiation environment and the human exposures that it creates.

INTRODUCTION

The CONTREC conference (Morrilton, AK, May 6–9, 2015) was a forum for discussion of the effects of ionizing radiation exposure on normal tissue. A unique situation involving normal tissue exposure is that experienced during space travel by healthy astronauts, and it is considered to be a limiting aspect of long-duration space missions, especially beyond low Earth orbit (*1*). This article describes the unique space radiation environment and its implications for health risks associated with space travel as adapted from a CONTREC lecture. It is intended as a primer for those unfamiliar with this topic.

[1] Address for correspondence: Loma Linda University, Department of Basic Sciences, Division of Radiation Research, Loma Linda, California 92354; email: grnelson@llu.edu.

HUMAN ENVIRONMENTS IN SPACE

The human environments in space can be associated with several mission architectures, which may be described in the form of reference missions. There are low Earth orbital missions aboard the International Space Station. There may be space operations in the vicinity of the Moon, such as in lunar orbit or at a stable gravitational point such as the L2 Lagrange point or with landing and surface operations. There may be operations at a near Earth asteroid (e.g., Asteroid Redirect Mission concept). Ultimately there may be Mars missions to a Mars moon (Phobos) or with landing on the Martian surface. Each mission concept is associated with time spent in space, location(s) traveled in space, vehicle design parameters (e.g., International Space Station and Orion Multipurpose Crew Vehicle) and extravehicular activities (in space suits) that define the radiation environments within the context of the solar system's status.

COMPLEX RADIATION FIELD

The radiation environment of the solar system is comprised of the full solar electromagnetic spectrum plus a complex mixture of charged particles (and their interaction products) derived from sources inside and outside of the solar system. Electromagnetic radiation is a negligible contributor to human exposure since spacecraft materials effectively shield against it (*2*). As for energetic charged particles, there are four primary sources: 1. galactic cosmic rays; 2. the Sun in steady state; 3. short-term solar emissions [solar particle events (SPEs)]; and 4. trapped radiation belts (Van Allen belts) around the Earth. The sum of these four sources determines the radiation at the surface of space vehicles or space suits and complex interactions with the spacecraft and space suit materials determines the environment at the surface of an astronaut's body. Figure 1 shows a visual snapshot of the radiation field during the Apollo 11 lunar mission as a micrograph of nuclear emulsion showing numerous tracks of protons and one heavy ion. The image is of a microscopic field with dimensions 140 × 165 microns.

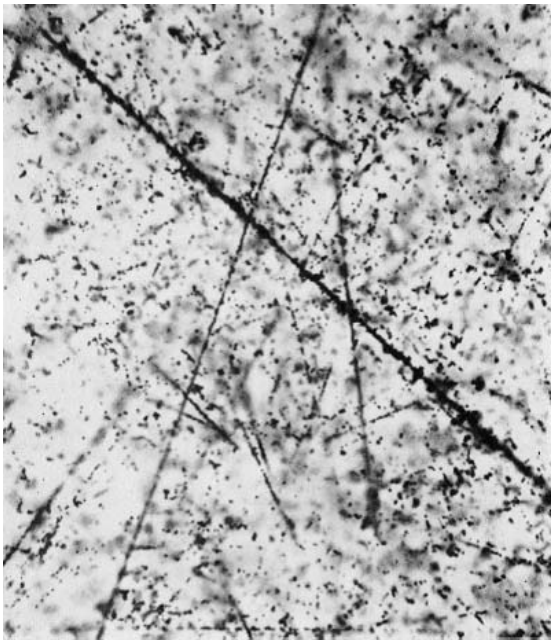

FIG. 1. An illustration of the ambient radiation exposure in deep space as a microscopic field of view of an Ilford G.5 nuclear emulsion that was worn on the ankle of Neil Armstrong during the Apollo 11 lunar landing mission in July, 1969. Individual silver grains due to gamma rays and electrons form a background against which numerous proton tracks can be seen, along with one track of a heavy ion with an estimated Z of 10–12. The 195 h flight briefly grazed the inner edges of the Van Allen belt and occurred during solar maximum of cycle 20. Reproduced and used with permission from Fig. 1 of Schaefer *et al*. (*36*)

PROPERTIES OF CHARGED PARTICLES

The properties of charged particles have been described in detail by many researchers. As one example, a very thorough review by Durante and Cucinotta (*1*) examines charged particles in a space environment context. Charged particles interact with materials primarily through Coulombic (charge–charge) interactions creating dense linear ''tracks'' of ionizations. The Bethe-Bloch formula [see Eq. 5.7 in Assessment of radiation exposure of astronauts in space. ICRP Publication 123 (*2*)] quantifies the differential energy loss (all mechanisms) by a particle moving through a medium as the stopping power, S. It can be used to calculate the energy loss along any segment of a track as a function of energy and target material composition and also to estimate the range in the material. The term, linear energy transfer (LET), is closely related to stopping power but is the differential energy *imparted* locally to target material by a charged particle per unit track length. LET, which is most commonly used to describe the quality of radiation, does not take into account energy imparted by the particle but transported away from the target material. LET is then dependent on the square of the charge (Z) of the particle (more accurately effective charge, Z^*, which is important for energies below a few MeV/n where the primary particle may pick up electrons from the material) and inversely with the square of the particle's velocity (v). By convention, the velocity is normalized to the speed of light (c) and is expressed as $\beta = v/c$. Thus LET is proportional to Z^2/β^2 (or Z^{*2}/β^2). By convention, energies of charged particles are normalized to mass to facilitate comparisons of particles of equal velocity. The units most commonly used are: 1. particle energy in MeV/n (million electron volts per atomic mass unit, denoted amu, u or n); and 2. LET in keV/μm (kiloelectron volts lost per micron of track length). Thus, a 150 MeV/n proton, $^{1}H^{1+}$, (representative solar particle event proton) has a velocity of $0.51 \times c$, an LET of 0.55 keV/μm (water) and a range of 15.6 cm in water. By comparison, a 1,000 MeV/n iron ion, $^{56}Fe^{26+}$, (representative galactic cosmic ray particle) has a velocity of $0.84 \times c$, an LET of 150.4 keV/μm and a range of 26.8 cm in water. It is important to note that an LET value does not define a unique particle configuration, as different combinations of charge and velocity can result in the same LET value. For example, a 2.2 MeV/n proton, $^{1}H^{1+}$, has an LET of ≈15 keV/μm and so does an 800 MeV/n $^{16}O^{8+}$ ion.

The Bragg curve describes the LET versus depth into material. As particles slow down near the end of their ranges, their LETs increase to a maximum (Bragg peak) before plunging to zero. Many examples of Bragg curves for experimental particle beams produced at the NASA Space Radiation Laboratory (NSRL) at Brookhaven National Laboratory (Upton, NY) can be found at the NSRL website (http://1.usa.gov/1To1SQs). The publicly available, NASA-developed computer program GERM can be used to determine various particle track parameters and plot Bragg curves (*3*).

The detailed three-dimensional structure of particle tracks varies with charge, energy and target material but is generally described as a cylindrical region surrounding the particle's trajectory having a densely ionizing ''core'' of 10–20 nanometers in diameter surrounded by a zone or ''penumbra'' of scattered electrons (also known as delta rays) whose average local ionization density decreases as 1/radius^2 and may extend out to about a centimeter. The average local dose generally drops below 10 cGy after 1–2 microns depending on the particle. The publicly available, NASA-developed computer program RITRACKS can be used to simulate particle tracks along with the chemical species they produce in water (*4*).

The dose delivered by charged particles to a macroscopic target is proportional to the particle number passing through a unit area (fluence, Φ) × LET and the spatial distribution of particles follows the Poisson distribution. The dose-to-fluence conversion is given as $D = \Phi \times \text{LET} \times k$, where D is in cGy, LET is in keV/μm, Φ is in cm^{-2} and k is 1.602×10^{-7} (assumes 1 cm thickness of water as the target). For example, a fluence of 10^6/cm^2 1,000 MeV/n iron particles (LET = 150.4 keV/μm) deposits a dose of 24.1 cGy. For 150 MeV/n protons of lower LET (0.55 keV/μm) the same dose is associated with a much higher fluence of 2.74×10^8/cm^2.

Charged particles also undergo nuclear interactions resulting in scattering or fragmentation into lighter (lower

TABLE 1
Galactic Cosmic Ray Composition for Selected Elements Commonly Used in NASA-Sponsored Accelerator Experiments (*5, 6*)

GCR composition for selected ions		Cycle 21/22 minimum Mewaldt (*5*)		Cycle 23/24 minimum ACE data (*6*)	
Z	Element	1 GeV/n		200 MeV/n	
1	H	3,000	91.092%	1,660	85.531%
2	He	270	8.198%	256	13.190%
6	C	6.40	0.194%	7.45	0.384%
8	O	5.93	0.180%	7.16	0.369%
14	Si	1.00	0.030%	1.00	0.052%
22	Ti	0.08	0.002%	0.10	0.005%
26	Fe	0.59	0.018%	0.65	0.033%

Notes. The relative abundances are normalized to silicon = 1. The absolute fluence for Si at 200 MeV/n is 11.1 $\times 10^{-8}$/(cm^2 s sr MeV/n) or 3.51/(cm^2 year sr MeV/n) ''cycle'' and ''minimum'' refer to so-called solar cycles and the stage of solar minimum defined below (*35*). GCR = galactic cosmic ray; ACE = advanced composition explorer (satellite).

Z) secondary particles, which typically have a greater range than the primary nuclei. The probability of nuclear reactions is dependent on particle energy and the detailed mechanisms of the many possible reactions.

GALACTIC COSMIC RAYS

Galactic cosmic rays (GCRs) are fully ionized atomic nuclei and other subatomic particles emitted by energetic sources outside of the solar system such as stars and highly energetic objects such as supernovae. GCR of $Z > 26$ are produced and accelerated by shock waves from supernovae. The abundance of GCRs by *Z* reflects the cosmic abundance of elements. By far the most abundant component is hydrogen nuclei or protons (numerically about 85%) followed by helium nuclei (about 13%) followed by other elements up to iron ($Z = 26$) with even-numbered elements such as ^{12}C, ^{16}O and ^{28}Si being more abundant than odd-numbered elements (*5*). Recent GCR composition data in several energy bands is available at the project website of the Advanced Composition Explorer (ACE) satellite which orbits about 1.5×10^6 km sunward of Earth, near the gravitationally-stable L1 Lagrange point (*6*). Data for selected particles at 200 MeV/n in 2007 from ACE along with earlier data for 1 GeV/n (*5*) from the Interplanetary Monitoring Platform (IMP) satellite are shown in Table 1. Both data sets are from solar minimum periods (see below) and the two energy bins span the energy range associated with the maximum fluence in the GCR energy distribution. The selected particles represent those most widely used in radiobiological investigations.

The energy spectrum of GCR ranges from <1 keV/n to over 10^5 MeV/n. Their median energy inside the solar system is ≈1,000 MeV/n. For convenience, GCRs of energy <30 MeV/n are often neglected in descriptions of space radiation environments because their ranges are so small that they would not pass through typical shielding levels. In the energy range from 1 to ≈1,500 MeV/n (accessible in particle accelerator facilities), the particle

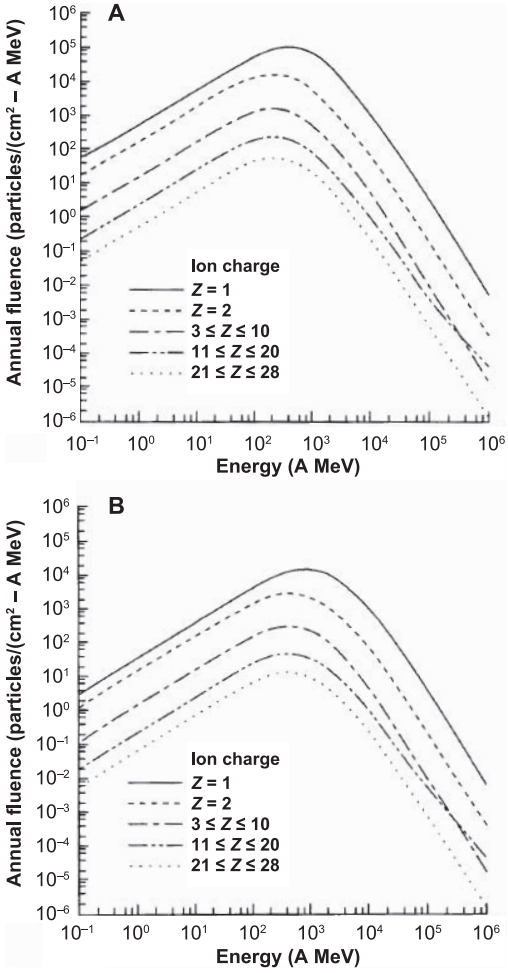

FIG. 2. Differential annual fluence spectra. Panel A: GCR ion fluence for 1977 solar minimum. Panel B: GCR ion fluence for 1981 solar maximum. Here energy has been multiplied by atomic number, A, rather than expressed as E/n. Note overall reduction in fluence but increase in energy of fluence maximum for solar max. Reproduced and used with permission from Fig. 1 of Wilson *et al.* (*37*).

abundance rises to a local maximum at ≈200–800 MeV/n followed by an exponential decline as shown in Fig. 2.

Galactic cosmic rays are isotropic in terms of direction and are steered by magnetic fields. The fluence and spectra of GCRs are under constant surveillance by many orbiting satellites and measurements have been obtained to distances beyond Pluto to the boundary of the heliosphere at ≈90–160 astronomical units (au; the average distance from Sun to Earth or 149,597,871 km) (*7*). The IMP and ACE satellites have generated the most comprehensive data sets for interplanetary magnetic fields and charged particles. GCR composition is found to be only weakly dependent on distance from the Sun (*5*). The GCR fluence and energy spectrum are modulated by solar activity corresponding to the 11-year solar cycle (see below). At solar maximum, the enhanced emission of solar wind and altered heliospheric magnetic field serve as a barrier to GCRs such that overall fluences are reduced; fluences of lower energy particle are reduced by over an order of magnitude (Fig. 2).

THE SUN

The Sun is the dominant source of radiation within the solar system. Its internal structure consists of a nuclear-burning core, followed by radiative and convection zones, and its visible ''surface'' is termed the photosphere. The Sun's atmosphere extends outwards through the corona and finally into the solar system as a low-density plasma (solar wind) of about 1 proton (plus electrons and other charged particles) per cm^3. Solar wind particles have energies in the range of 0.5–2 keV/n and velocities of ≈300–900 km/s (*8*), but they have such short ranges in aluminum or plastic shielding materials that they pose little health hazard (<0.1 micron calculated with the publicly available ''PSTAR'' program (http://1.usa.gov/1oGCFUD). The steady solar wind emission is distinct from the short-term ejections of higher energy material from the Sun (solar particle events), discussed below.

MAGNETIC FIELDS AND RADIATION BELTS

Charged particles are acted upon by magnetic fields according to the Lorentz force, which accelerates them perpendicular to their direction of motion, causing them to spiral along magnetic field lines. Magnetic fields are the major determinant of charged-particle spatial distributions in interplanetary space. The magnetic field at the Earth's surface varies by location with the lowest values <24 μT (0.24 Gauss) over the South Atlantic Ocean and Southern Brazil to highest values exceeding 60 μT (0.6 G) south of Australia and over Siberia; over most of the Earth's surface the values are from 30–50 μT (*9*). This reflects the fact that the approximately dipole field is offset from the center of the Earth. These fields trap protons and electrons in annular inner and outer radiation belts (Van Allen belts), which at the equator extend from ≈200 km out to 40–60,000 km above Earth's surface. The proton belt intensity peaks at about 5,000 km (for 10 MeV protons) while inner and outer electron belts peak in intensity at 3,000 and 20,000 km. The weaker field area defines the South Atlantic Anomaly over which the trapped radiation belts of protons dip to lower altitudes and is responsible for enhanced exposure to protons during the period when spacecraft are in low-Earth orbit. Exposure rates at International Space Station orbits are about 233 μSv/day with 166 μSv/day coming from trapped radiation (*10*).

Outside the Earth's atmosphere, the solar wind distorts the field by pushing in the sun-facing side and extending the opposite side into an elongated ''magnetotail'' almost a million miles long (*8*). The resulting geomagnetic field is responsible for the geometry of the trapped radiation belts and relative shielding of spacecraft traveling in low-Earth orbit. The movement of particles into the geomagnetic field is determined by the field strength and the particle velocity. Trajectories of particles with energies less than a particular threshold (geomagnetic cutoff, E_0) will be bent along arcs and sent back out of the geomagnetic field. Those of energy $>>E_0$ will travel in straight lines into the atmosphere and those of intermediate energies $>E_0$ will travel in curved paths before reaching the atmosphere and may be trapped into the radiation belts. However, most trapped protons derive from interactions with the atmosphere.

At a global scale, the Sun has an essentially dipolar magnetic field with a field strength of about 1,000 μT (10 G) at the surface. The orientation of this field reverses every 11 years and completes a full 22-year ''Hale'' cycle to restore the field to its original orientation (*11*). The interplanetary field strength is about 5 nT (50 microgauss) at the Earth's orbit and decreases with distance (*8*). The field takes on the form of an Archimedean spiral (''Palmer spiral'') in the plane of the solar system due to the rotation of the Sun and propagation of solar wind. The spiral field lines guide the trajectories of charged particles emanating from the Sun's atmosphere as solar wind or solar particle events (see below). The preferential corridors for particles along field lines are called flux tubes (see Fig. 3).

SOLAR CYCLE

The luminosity of the Sun changes with a regular periodicity of ≈11 years, referred to as the solar cycle, which is coupled to reversals of the magnetic field as described above. At solar maximum the stream of charged particles is greater than at solar minimum. The outward flow of material carries with it additional current and enhanced heliospheric magnetic fields, which have the effect of blocking the inward flow of cosmic rays from outside the solar system. So at solar maximum, GCR fluence is reduced, especially at lower particle energies. However, at solar maximum the solar surface is more dynamic in terms of mass transport and magnetic field rearrangement, which is manifested by the appearance of sunspots and ejection of

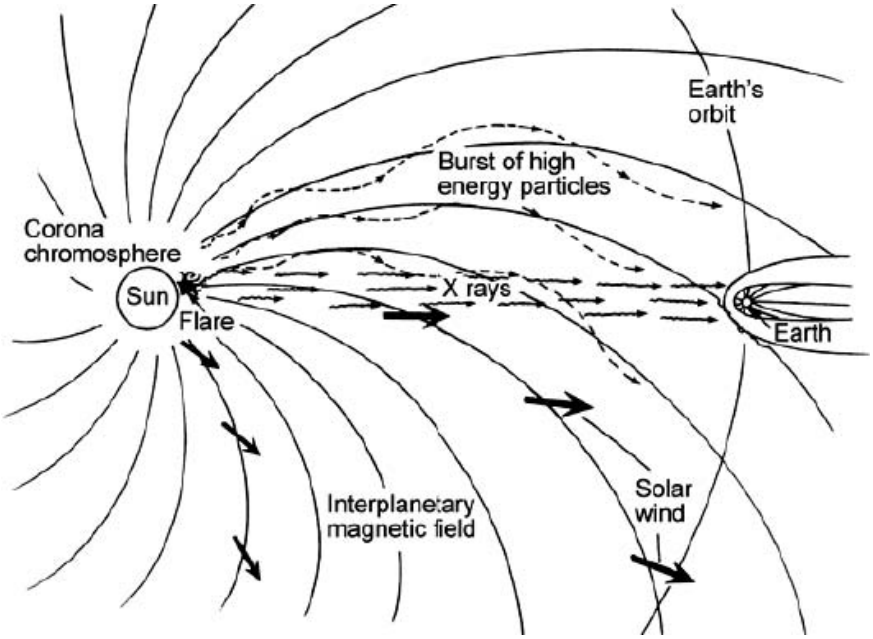

FIG. 3. Interplanetary magnetic field, as originating in the Sun and as deformed by the effects of the solar rotation and solar wind. Reproduced and used with permission from Fig. 3.15, NCRP Report No. 153 (*7*).

mass as solar particle events (see below). Occasional sunspots have been observed since ancient times but they have been telescopically observed for 400 years and systematically recorded since 1755, from which time cycles have been numbered. Solar cycle 23 peaked (solar maximum) between 2000 and 2002. Solar cycle 24 began on January 4, 2008 at the first appearance of a sunspot with magnetic polarity reversed from the prior cycle. The enhanced luminosity of the Sun at solar maximum also results in greater heating of the Earth's outer atmosphere, which can increase drag on low-Earth orbit spacecraft.

SOLAR PARTICLE EVENTS

The National Oceanographic and Atmospheric Administration Space Environment Center defines a solar particle event (SPE) as the occurrence of integral particle flux, mainly energetic protons, over a period of time with energy greater than 10 MeV that exceeds 10 particles/(s – cm^2 sr) (*12*). The term ''SPE'' replaces the older and less precisely defined term ''solar flare'', which should correctly be used to refer to events associated with X-ray emissions. The occurrence of SPEs of all sizes are random, but their occurrences are more frequent during solar maximum than solar minimum. Small events may occur at a frequency of ≈1,000 per year at solar maximum versus ≈10 per year for large events (*13*) and last from hours to a few days. Kim *et al.* (*14*) evaluated the probability of occurrence of solar particle events in solar cycles 19–23 as a function of event size measured as integral fluence of protons of energy >30 MeV. They found that while 50% or more of the events had sizes in excess of 10^7 particles/cm^2, less than 8% had event sizes of 10^9/cm^2. SPEs consist predominantly of protons with kinetic energies from <1 MeV up to a few hundred MeV.

Solar particle events are grouped into two classes. The smaller, shorter events are termed impulsive events (or impulsive flares). These events derive their material from the lower solar atmosphere where the particles are accelerated through interactions with gradients of rearranging magnetic fields originating in sunspots or from other convective movements of plasmas. The angular dependence of the impulsive events is relatively small so that their particles follow flux tubes along interplanetary field lines. Events with speeds comparable to solar wind follow an Archimedean spiral length of ≈1.3 astronomical units. If the Earth lies along the field lines followed by the event ejecta, the event is said to be ''well connected''. Most well-connected impulsive flares originate at 50–70° solar longitude (*13*).

The larger events, referred to as gradual events or coronal mass ejections (CMEs), are much larger. They are associated with broad angular emissions of particles and, in addition to magnetic field gradient acceleration, are also associated with shock wave acceleration of particles in the Sun's outer atmosphere or corona. Transit speeds of ejecta to Earth are only loosely correlated with CME speeds determined partly by the solar wind conditions between the Sun and Earth. For example, CMEs with speeds of ≈500 km/s may have transit times to Earth of 2.5–4.5 days (*15*). They do not need to be well connected for their particles to reach the vicinity of Earth. CMEs eject around 1–10 × 10^{15} g of material at 100–3,000 km/s (*13*) and the current and induced magnetic fields they generate at the Earth's surface are sufficient to disrupt electrical power grids as well as

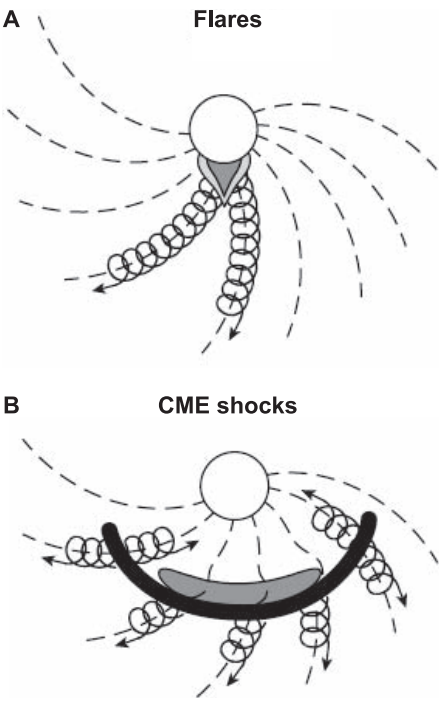

FIG. 4. Panel A shows the propagation paths of impulsive SPEs following the Parker spiral field lines, while panel B shows the wide angular dependence of CMEs. Reproduced and used with permission from Fig. 2.1 of Reames (*13*).

damage satellites. For example, a large 1989 CME shut down the Hydro-Quebec power system in Canada for more than 8 h (*16*). Over polar latitudes particles (protons and electrons) from SPEs may ionize gases in the high atmosphere (100–300 km) leading to the familiar aurorae, where red, green and bluish colors are due to ionization of atomic and molecular oxygen and nitrogen. During solar minimum there may be about 1 CME per week whereas at solar maximum there may be 2–3 per day (*13, 17*). These events are capable of compromising human health in space travelers. The largest of these, known as the ''Carrington event'', occurred in 1859 and was associated with an optical flare visible to the naked eye in daytime and had an estimated omnidirectional fluence of 1.8×10^{10} particles/cm^2 for energies >30 MeV. Figure 4 shows the different geometries of impulsive flares and coronal mass ejections and their associations with field lines.

Because they derive material from different parts of the Sun's atmosphere, the compositions of impulsive versus gradual events also differ and impulsive events are enriched in heavier elements, shown in Table 2. The energy spectra of SPEs differ substantially from that of GCRs. The maximum energies are generally <250 MeV/n and the differential fluence decreases continuously with increasing energy. The majority of SPE particles are stopped by relatively thin layers of shielding, which limits their health hazards except to tissues near the body surface and during spaceflight operations outside vehicles. Several very large CMEs have been well characterized and serve as reference standards for worst-case scenarios in risk assessment for which both total fluence and the fraction of the fluence at high energy (''hardness of the spectrum'') are important. Figure 5 shows the differential fluence versus energy spectra for six large CMEs. Note how effectively 4.3 and 15 mm shielding thicknesses of aluminum would attenuate the majority of the protons of energies below 30 or 60 MeV/n. Figure 6 further shows the mitigation of SPEs by different shielding thicknesses of an arbitrary material. Fluence (at the lunar surface) and energy have been converted to dose equivalent [at deep tissue locations or blood-forming organs (BFOs)] plotted against the time course of the August 1972 event. Shielding thickness is given in ''areal density'' units of g/cm^2, which can be converted to actual thicknesses by dividing by a specific material's density (e.g., 2.70 g/cm^3 for aluminum). Shielding thickness of 0.3 g/cm^2 would correspond to a spacesuit while 30 g/cm^2 would correspond to a safe haven in the interior of a space vehicle (including wall-mounted equipment panels, etc.) while 5 and 10 g/cm^2 would be representative of rovers and nominal shielded areas of spacecraft.

TABLE 2
Comparison of the Average Compositions of Solar Atmosphere (Visible Surface Region of the Solar Atmosphere is the Photosphere), Gradual SPEs (Coronal Mass Ejections), Impulsive SPEs and Galactic Cosmic Rays for Selected Abundant Elements

Element	Z	Photosphere (%)	CMEs (%)	Impulsive SPEs (%)	GCRs (%)
H	1	90.97	96.36	95.22	86.91
He	2	8.90	3.50	4.38	11.74
C	6	0.032	0.029	0.041	0.421
O	8	0.067	0.061	0.095	0.499
Ne	10	0.011	0.009	0.038	0.062
Mg	12	0.003	0.012	0.039	0.103
Si	14	0.003	0.009	0.034	0.098
Ti	22	0.000	0.000	0.000	0.002
Fe	26	0.003	0.008	0.103	0.003
Other	Other	0.012	0.013	0.054	0.167

Notes. The enhancement in abundance for $Z \geq 2$ in impulsive events is relative to CME but the relative paucity of $Z \geq 2$ particles is relative to GCR. Data used with permission from ref. (*13*). CMEs = coronal mass ejections; SPEs = solar particle events; GCRs = galactic cosmic rays.

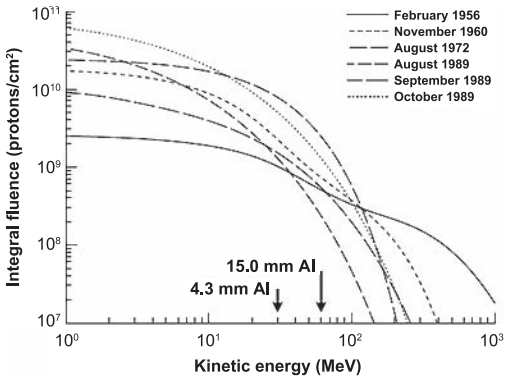

FIG. 5. Large SPE integral fluence (sum of all fluence below an energy value) spectra at 1 au. Arrows indicate ranges in aluminum for protons of energy 30 and 60 MeV/n. For these events, total fluence for energies >30 MeV ranged from 2×10^8 to 8×10^9. Modified and used with permission from Fig. 3 of Wilson *et al*. (*38*).

Parsons and Townsend (*18*) calculated dose rates for the August 1972 event behind 1, 2 and 5 g/cm^2 shielding. They found that peak dose rates to the skin, eye and bone marrow could reach 1.4 Gy/h, 0.9 Gy/h and 8.5 cGy/h, respectively, behind 1 g/cm^2 shielding. Behind 5 g/cm^2 these values would be reduced to 21 cGy/h, 20 cGy/h and 6 cGy/h but cumulative doses to eye and skin could exceed 2 Gy. Turner (*19*) has estimated that large CMEs such as the February 1956, November 1960, August 1972 and October 1989 events had the capacity to generate integral doses (over the entire event time course) of $\geq$10 cGy/Eq to BFOs behind 10 g/cm^2 shielding and may exceed NASA's 30-day exposure limits or approach annual limits behind only spacesuit level shielding of 0.3 g/cm^2. Of some 400 SPEs observed since 1955 only 41 had integral fluences exceeding 10^8/cm^2 (for particles of energy >30 MeV/n), which corresponds roughly to 1 cGy in tissue (*20*). Exposures to cosmic rays and SPEs at the surface of the Earth are blocked by the atmosphere, which has an areal density of $\approx$1,000 g/cm^2 (*2*).

EXPOSURE LEVELS AND RISK ESTIMATION

Galactic cosmic ray ions are able to penetrate several tens of centimeters of materials such as aluminum or tissue (water) and nuclear interaction between GCR particles and target nuclei will produce lower Z secondary particles whose lower LETs confer greater range than the primary particles. As a consequence, practical levels of shielding materials will not fully absorb all space radiation, and there will be unavoidable exposures to be kept to a minimum. NASA has estimated that exposures will result in each of an astronaut's cells (assuming $\approx$100 um^2 projected area or geometric cross section) being ''hit'' (traversed) by a proton once every three days, a helium nucleus once every few weeks and a heavy ion ($Z > 2$) once every few months (*21*). The particle spectrum and fluence rates will result in deep-space tissue dose- and dose-equivalent rates of around 0.3–0.6 mGy/day and 1–1.8 mSv/day, respectively; these estimates have been directly verified by the Mars Science Laboratory spacecraft (*22*). However, the long track ranges mean that very large numbers of cells in cylindrical volumes around the tracks will be simultaneously traversed, so that the ''hit'' kinetics are nonrandom and functional units of multiple cells may not respond independently.

NASA has estimated exposure levels for a set of design reference missions that are engineering-based overviews of conceptual missions and include destinations in cis-lunar space, lunar surface outposts, asteroids, as well as Mars and its moons (*23*). They take into account location in space, mission duration, operations and vehicle design and shielding. Sophisticated computer simulations (radiation transport codes) then utilize space radiation environment models (*10, 24, 25*) to project mission exposures to the interior of vehicles. Computerized anatomical models of human bodies further enable exposure estimates for organs and tissues. Finally, radiobiological and epidemiological data and models are used to estimate adverse consequences of exposures. This information has been synthesized by expert panels into recommendations for spaceflight agencies to aid in estimating health risks and identifying mitigation or countermeasure strategies (*2, 7, 26*). Current exposure estimates by NASA for different reference missions assuming 10 g/cm^2 shielding and ICRP 60 quality factors (*27*) are as follows: 1. low-Earth orbit 6–12 months, 50–100 mSv (1/3 from protons and 2/3 from GCRs); 2. deep-space sortie – 1 month, 32.1 mGy/Eq with 16.7 mGy from GCRs; 3. lunar visit/habitat, 231 mGy/Eq with 120–150 mGy from GCRs; 4. deep-space journey – 1 year: 385 mGy/Eq with 200 mGy from GCRs; and 5. Mars mission at solar minimum (approximately 3 years), 1.0–1.2 Sv (245–360 mGy) comprised of 130–180 mGy protons, 45–70 mGy He, 20–40 mGy $3 < Z < 9$ particles, 30–40 mGy $Z > 10$ particles and 20–30 mGy neutrons and other particles. These estimates incorporate many assumptions and are constantly updated and revised.

NASA has identified four major categories of risk from space radiation exposure. These are: 1. carcinogenesis; 2. degenerative tissue risk (e.g., cardiovascular disease); 3. acute (during a mission) and late (after a mission) risks to the central nervous system (CNS); and 4. acute radiation syndromes. Research activities for these risks are related to a codified set of research questions (*28*). Perhaps the best developed risk model for space radiation is NASA's NSCR 2012 model for cancer risks that projects cancer incidence and mortality incorporating mission design parameters, epidemiological data, radiation fields, dose rates and quality factors, and establishes a probability distribution for risk of exposure-induced death that enables estimates of uncertainty (*29*). NASA establishes a cancer exposure limit such that ''planned career exposure to ionizing radiation shall not exceed 3 percent Risk of Exposure-Induced Death (REID) for cancer mortality at a 95 percent confidence level'' (*30*). The many components of uncertainty are dominated by

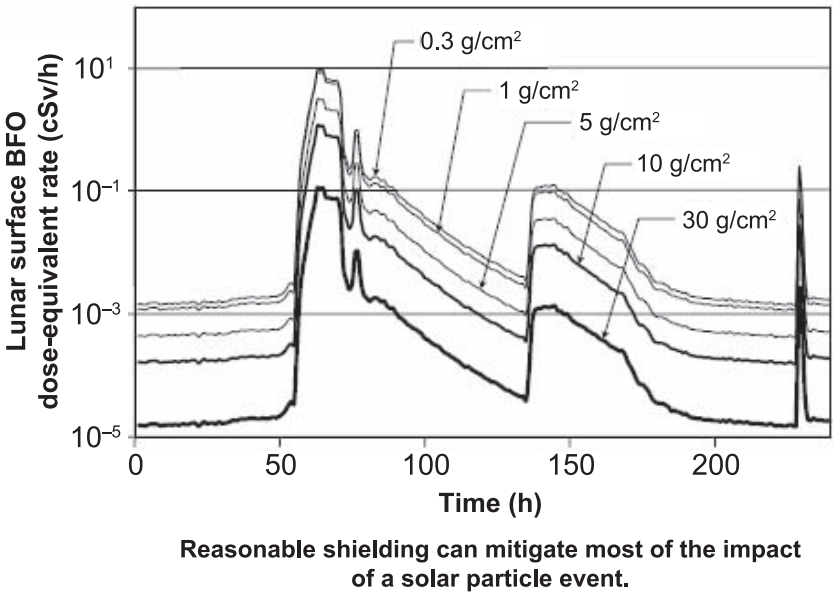

FIG. 6. Time course of lunar surface dose equivalent rate for blood-forming organs and effects of aluminum shielding for the large SPE on August 2, 1972. This event occurred between the Apollo 16 and 17 missions. Blood-forming organs dose equivalents are based on NCRP Report No. 132 recommendations (*26*). Note the high-dose-rate period of ≈20 h immediately after arrival of charged particles. Reproduced and used with permission from Fig. 4 of Turner (*19*).

biological issues such as quality factors, dose-rate effectiveness factors, rules for combining effects from multiple ion types and their order of exposure and modifying effects of other spaceflight environmental features such as low gravity, confinement and isolation stress, sleep deprivation, etc. For noncancer risks, permissible exposure limits (PELs) for short-term and career exposures to space radiation have been approved by NASA and set requirements and standards for mission design and crew flight assignment (*30*). Current PELs are shown in Table 3 [modified from ref. (*30*)]. Because tissue-weighting factors are not well established for the CNS, values are given in Gy rather than Gy/Eq.

Ground-based experiments with charged particles using appropriate biological models are critical in establishing dose responses, dose-rate effects and dependence on track structure. To date, most ground-based experiments have involved acute exposures to beams of single-energy accelerated ions. The NSRL at Brookhaven National Laboratory has been the focus of such studies in the U.S. since the late 1990s. It provides a series of beams from protons to iron ions with energies up to 1 GeV/n with an ongoing upgrade to 1.5 GeV/n for heavy ions (*31*). Importantly, there are ongoing activities directed at extending experimental capabilities to simulate a multiple-ion GCR spectrum and to protract dose (*32, 33*). Although these simulations will be limited by accelerator facility operational capabilities, they will nevertheless allow researchers to simulate a mixed field in tissue that will be dominated by protons and helium ions along with selected heavy ions as would be found in the interior of spacecraft and human bodies due to radiation shielding and transport (*32*). The

TABLE 3
Permissible Exposure Limits Used by NASA to Set Requirements and Standards for Mission Designs and Crew Flight Assignments

	Permissible exposure limits in Gy or Gy/Eq. (*30*)		
Target organ	30-day exposure limit	1-year exposure limit	Career exposure limit
Lens	1.0 Gy/Eq	2.0 Gy/Eq	4.0 Gy/Eq
Skin	1.5 Gy/Eq	3.0 Gy/Eq	6.0 Gy/Eq
BFOs	0.25 Gy/Eq	0.50 Gy/Eq	No applicable
Heart	0.25 Gy/Eq	0.50 Gy/Eq	1.0 Gy/Eq
CNS	0.50 Gy	1.0 Gy	1.5 Gy
CNS ($Z \geq 10$ contribution)	Not specified	0.10 Gy	0.25 Gy

Note. CNS = central nervous system; BFOs = blood-forming organs.

contributions to exposure from neutrons are also considered in simulation models. While neutrons decay with a half life of about 10 min in free space they are produced abundantly by interactions of charged particles with thick shielding (*34*).

SUMMARY

The space radiation environment is a complex mixture of radiation species dominated by highly-penetrating charged particles from the Sun and sources outside the solar system. Their energy spectrum and abundances are modified by interplanetary magnetic fields, long-term solar activity and punctuated by short-term solar particle events. From the properties of charged particles and the composition of the environment associated with conceptual missions and vehicles, transport codes model the radiation fields that would be experienced by astronauts during different missions. Finally, risk models based on epidemiological methods and radiobiological data from accelerator experiments use the predicted fields to estimate health risks and guide safe spaceflight operations. Cumulative doses to astronauts expected for Mars design reference missions approach 1 Gy and can be in conflict with current permissible limits, emphasizing the need for a more thorough understanding of biological responses to charged particles.

ACKNOWLEDGMENTS

The information contained in this article was presented at CONTREC (Conference on Normal Tissue Radiation Effects and Countermeasures), May 6–9, 2015, at Winthrop Rockefeller Institute in Morrilton, Arkansas. This work was supported by NASA (grant no. NNX10AD59G) and NSBRI (grant no. RE03701) through NASA cooperative agreement NCC 9-58.

Received: November 3, 2015; accepted: December 18, 2015; published online: March 28, 2016

REFERENCES

1. Durante M, Cucinotta F. Physical basis of radiation protection in space travel. Rev Modern Phys 2011; 83:1245–81.
2. Task Group on Radiation Protection in Space, ICRP Committee 2, Dietze G, Bartlett DT, Cool DA, Cucinotta FA, Jia X, et al. Assessment of radiation exposure of astronauts in space. ICRP Publication 123. Ann ICRP 2013; 42:1–339.
3. Cucinotta F, Plante I, Ponomarev A, Kim MY. Nuclear interactions in heavy ion transport and event-based risk models. Radiat Prot Dosimetry 2011; 143:384–90.
4. Plante I, Ponomarev A, Cucinotta F. 3D visualisation of the stochastic patterns of the radial dose in nano-volumes by a Monte Carlo simulation of HZE ion track structure. Radiat Prot Dosimetry 2011; 143:156–61.
5. Mewaldt, R. Elemental composition and energy spectra of galactic cosmic rays. In: Feynman J, Gabriel S, editors. Interplanetary particle environment: Proceedings of a conference. JPL Publication 88–28l. Pasadena: National Aeronautics and Space Administration; 1988. p. 121–134. (http://go.nasa.gov/1POs0Ov)
6. ACES 2015 Advanced Cosmic Explorer database. Pasadena: California Institute of Technology. (bit.ly/1XPYVYe)
7. Information needed to make radiation protection recommendations for space missions beyond low-earth orbit. NCRP Report No. 153. Bethesda: National Council on Radiation Protection and Measurements; 2006.
8. Vallée J. Observations of the magnetic fields inside and outside the solar system: From meteorites (~10 attoparsecs), asteroids, planets, stars, pulsars, masers, to protostellar cloudlets (< 1 parsec). Fundamentals of Cosmic Physics 1998; 19:319–422.
9. Finlay C, Maus S, Beggan C, Bondar T, Chambodut A, Chernova T, et al. International geomagnetic reference field: The eleventh generation. Geophys J Int 2010; 183:1216–30.
10. Badavi F, Walker S, Santos Koos L. Evaluation of the new radiation belt AE9/AP9/SPM model for a cis lunar mission. Acta Astronautica 2014; 102:156–68.
11. Thomas S, Owens J, Lockwood M. The 22-year Hale cycle in cosmic ray flux -evidence for direct heliospheric modulation. Solar Phys 2014; 289:407–21.
12. Aghara S, Sriprisan S, Singleterry R, Sato T. Shielding evaluation for solar particle events using MCNPX, PHITS and OLTARIS codes. Life Sci Space Res 2015; 4:79–91
13. Reames, D. Particle acceleration at the Sun and in the heliosphere. Space Sci Rev 1999; 90:413–91.
14. Kim Y, De Angelis G, Cucinotta F. Probabilistic assessment of radiation risk of astronauts in space missions. Acta Astronaut 2011; 68:747–59.
15. Cane H, Richardson I, St. Cyr O. Coronal mass ejections, interplanetary ejecta and geomagnetic storms. Geophysical Res Lett 2000; 27:3591–4.
16. Baker D. How to cope with space weather. Science 2002; 297:1486–7.
17. Solar physics, coronal mass ejections. Washington, DC: NASA; 2015. (http://go.nasa.gov/1fXnjDa)
18. Parsons J, Townsend L. Interplanetary crew dose rates for the August 1972 solar particle event. Radiat Res 2000; 153:729–33.
19. Turner R. Space weather challenges intrinsic to the human exploration of pace. In: Gopalswamy N, Mewaldt R, Torsti J, editors. Solar eruptions and energetic particles geophysical monograph series no. 165: Washington, DC: American Geophysical Union; 2006. p. 367–74.
20. Cucinotta F, Kim MY, Chappell L. Evaluating shielding approaches to reduce space radiation cancer risks. Washington, DC: 2012; NASA Technical Memorandum TM-2012-217361.
21. Human exploration research opportunities. Appendix D. NNJ14ZSA001N-Radiation. Ground based studies in space radiobiology. Catalog of Federal Domestic Assistance (CFDA) No. 43.003. Washington, DC: NASA Space Radiation Program Element; 2015. (http://nspires.nasaprs.com/)
22. Zeitlin C, Hassler D, Cucinotta F, Ehresman, B, Wimmer-Schweingruber R, Brinza D, et al. Measurements of energetic particle radiation in transit to Mars on the Mars science laboratory. Science 2013; 340:1080–4.
23. Pathways to exploration - rationales and approaches for a U.S. Program of Human Space Exploration. National Academy of Sciences, National Research Council. Washington, DC: National Academies Press; 2014.
24. O'Neill, P. Badhwar - O'Neill 2010 galactic cosmic ray flux model - Revised. IEEE Trans Nucl Sci 2010; 57:3148–53.
25. Mrigakshi A, Matthiä D, Berger T, Reitz G, Wimmer-Schweingruber R. How galactic cosmic ray models affect the estimation of radiation exposure in space. Adv Space Res 2013; 51:825–34.
26. Radiation Protection Guidance for Activities in Low-Earth orbit. NCRP report 132. Bethesda: National Council on Radiation Protection and Measurements; 2000.
27. Recommendations of the International Commission on Radiological Protection. ICRP publication 60. Ann ICRP 1991; 21:1–3.
28. Human research roadmap. Washington, DC: NASA; 2015. (http://humanresearchroadmap.nasa.gov/)

29. Cucinotta F, Chappell L, Kim, M. Space radiation cancer risk projections and uncertainties. NASA Technical Paper 2013–217375. Washington DC, 2013.

30. NASA space flight human system standard. Volume 1: Crew health. NASA-STD-3001. Washington, DC: NASA, 2007.

31. Lowenstein D, Rusek A. Proceedings of the 4th IWSRR. Technical developments at the NASA Space Radiation Laboratory. Radiat Environ Biophys 2007; 46:91–4

32. Slaba T, Blattnig S, Norbury J, Rusek A, La Tessa C, Walker, S. GCR simulator reference field and a spectral approach for laboratory simulation. NASA Technical Paper 2015-218698. Washington, DC: National Aeronautics and Space Administration; 2015.

33. Kim MY, Rusek A, Cucinotta F. Issues for simulation of galactic cosmic ray exposures for radiobiological research at ground-based accelerators. Front Oncol 2015; 5:122.

34. Norbury J, Slaba T. Space radiation accelerator experiments - The role of neutrons and light ions. Life Sci Space Res 2014; 3:90–4.

35. George J, Lave K, Wiedenbeck M, Binns W, Cummings A, Davis A, et al. Elemental composition and energy spectra of galactic cosmic rays during solar cycle 23. Astrophys J 2009; 698:1666–81.

36. Schaefer H, Benton E, Henke R, Sullivan, J. Nuclear track recordings of the astronauts' radiation exposure on the first lunar landing mission Apollo XI. Radiat Res 1972; 49:245–71.

37. Wilson, J, Cucinotta, F, Tai, F, Simonsen, L, Shinn, J, Thibeault, S, Kim, M-Y. Galactic and solar cosmic ray shielding in deep space. NASA Technical Paper NASA TP-3682. Washington, DC: NASA, 1997.

38. Wilson J, Shinn J, Simonsen L, Cucinotta F, Dubey R, Jordan W, et al. Exposures to solar particle events in deep space missions. NASA Technical Paper NASA TP-3668. Washington, DC: NASA, 1997.